Inorganic Chemistry

pubs.acs.org/IC
Article

Design of Core@Shell Nanoparticles Based on Gold and Magnetic NiFe Prussian-Blue Analogues Featuring Shape-Dependent Magnetic and Electrochemical Activity

Shoaib Azeem, Joaquín Soriano-López, Isaac Brotons-Alcázar, Christopher Allen, Ramón Torres-Cavanillas,* Roger Sanchis-Gual,* and Eugenio Coronado*

Cite This: *Inorg. Chem.* 2025, 64, 6510−6518

ABSTRACT: Au@Prussian-Blue analogue (PBA) core@shell nanoparticles (NPs) are highly versatile nanostructures with complementary and shape-dependent properties of interest in the current technologies. However, due to the high reactivity of cyanides toward Au, scarce PBAs have been successfully synthesized in direct contact with Au NPs, leaving the formation of anisotropic Au@PBA NPs as a significant synthetic challenge. Here, we have developed a robust protocol for synthesizing core@shell NPs, composed of a magnetic $CsNi[Fe(CN)_6]$ PBA shell grown on individual Au NPs, regardless of the core morphology (spheres, rods, or stars). Specifically, the uniqueness of our protocol lies in the prior Au core functionalization with anchoring molecules that facilitate PBA growth while preventing Au etching and preserving the initial oxidation states of the metals. This has afforded direct growth of ferromagnetic $Ni^{II}Fe^{III}$ PBAs on Au NPs. Moreover, by exploiting the structural mismatch at the Au/PBA interface and the curvature of anisotropic Au templates, we manage to induce a substantial structural strain within the PBA shell. When star-shaped Au nanoparticles are used, a maximum strain of 2.0% is reached. This strain combined with an increased polycrystallinity lead to modifications in the PBA catalytic properties, resulting in a 10-fold improvement in the intrinsic electrocatalytic activity.

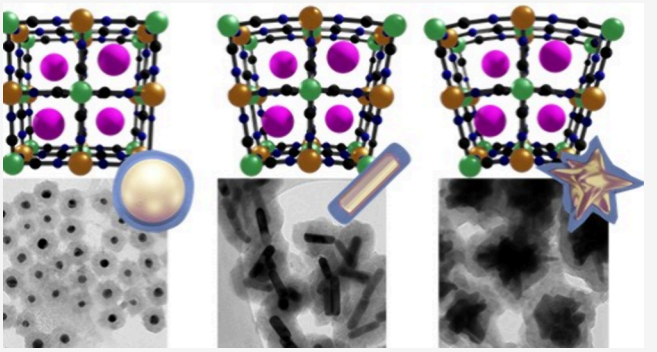

1. INTRODUCTION

The synthesis of core@shell hybrid nanomaterials that combine coordination polymers with other inorganic compounds is an attractive approach to enhance or even give rise to new physical properties thanks to the strong interaction occurring at their interface.[1−6] One of the most exciting core@shells are those composed of a Au core and bimetallic cyanide-bridged coordination polymers, known as Prussian Blue analogues (PBAs). These compounds, with a general formula of $AM^{II}[M'^{III}(CN)_6]\cdot nH_2O$ (in short $M^{II}M'^{III}$), where A represents alkali cations and M and M' transition metal ions, are very promising in biomedicine, magnetism, or catalysis due to their chemical versatility and property tunability.[7−14] In this regard, the presence of a gold core can result in a remarkable enhancement of the PBA intrinsic properties and additional synergistic effects.[4,15,16] For example, core@shell structures based on the classical Prussian Blue (PB) $Au@Fe^{III}Fe^{II}$ have been extensively explored for theragnostic, owing to the PB strong photothermal conversion, combined with the contrast agent capabilities of Au.[17,18] The preparation of $Au@Fe^{III}Fe^{II}$ is relatively simple, requiring only the in situ reduction of $[Fe^{III}(CN)_6]^{3-}$ on the Au surface in the presence of Fe^{III} ions. However, this scenario is far more complex for obtaining other PBA shells in their pristine form ($M^{II}M'^{III}$), since it requires the hexacyanometalate in the oxidation state of +3. Therefore, this previous protocol hampers the growth of PBAs with interesting magnetic and catalytic properties such as $Ni^{II}Fe^{III}$. As a result, researchers have delved into different synthetic methods for fabricating Au@PBA heterostructures that use cyanides as anchoring sites for the PBA overgrowth. Regrettably, these protocols consistently lead to (i) Au etching, triggered by precursor cyanides,[19] which is particularly dramatic for anisotropic NPs[20]; (ii) the formation of the reduced version of the intended PBA because of the use of reductants to prevent Au etching.[15,21,22] Thus, more protocols for synthesizing nonreduced PBAs in direct contact with Au NPs are required to properly exploit all their potential synergetic effects.

Received: December 13, 2024
Revised: February 26, 2025
Accepted: March 4, 2025
Published: March 26, 2025

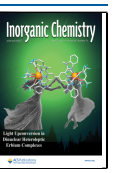

To tackle this synthetic challenge, we envisage the use of anchoring molecules different from cyanide to prevent Au etching while facilitating the subsequent growth of the PBA. This strategy has been demonstrated to be useful for forming other coordination polymers around Au nanostructures.[23,24] Notably, mercaptopyridine (MPy) molecules have been found to be efficient anchoring points for the formation of a cyanide-based molecular material on Au substrates.[25] Hence, in this work, we designed a novel protocol using MPy for preparing Au@$Ni^{II}Fe^{III}$ core@shell NPs. Our synthetic strategy is general and versatile, enabling the formation of nonreduced PBA over Au anistropic cores, which can be of interest in fields such as magnetoplasmonics or molecular electronics thanks to the intimate contact between the plasmonic core and magnetic shell.[23,26] Interestingly, we found that depending on the Au shape, the PBA grows with different degrees of polycrystallinity and strain within its structure, reaching the highest strain levels in the star-shaped NPs. Both effects lead to important modifications of the shell electrocatalytic properties. In particular, when using stars, the PBA intrinsic electrocatalytic activity toward the oxygen evolution reaction (OER) was improved by approximately 10-fold compared to that of the pristine material.

2. EXPERIMENTAL SECTION

2.1. Materials. All chemical reagents were purchased and used without further purification. Silver nitrate was purchased from Alfa Aesar. Chloroauric acid, L-ascorbic acid, potassium iodide, sodium citrate tribasic dihydrate, hexadecyltrimethylammonium bromide (CTAB), sodium borohydride, 4-mercaptopyridine 95%, cesium chloride, nickel(II) chloride, and potassium hexacyanoferrate were purchased from Sigma-Aldrich. Ultrapure water (18.2 MΩ) was used in the following syntheses. The reagents used in this work do not require any specific protocol to control their risks.

2.2. Synthesis of NPs.

1. Au Nanospheres (NSp) were synthesized following the standard Turkevich's method.[27] To 100 mL of boiling 0.5 mM $HAuCl_4$ solution was added 5 mL of 10 mg/mL sodium citrate solution. The solution briefly turned faint gray before becoming deep red wine within 2−5 min, indicating the successful formation of colloidal Au.
2. Au Nanorods (NRd) were obtained through a seed-mediated growth method.[28] First, 25 μL of 50 mM $HAuCl_4$ solution was added to 4.7 mL of CTAB 0.1 M, and the mixture was stirred at 30 °C for 5 min. Next, 300 μL of a freshly prepared $NaBH_4$ 10 mM solution was rapidly injected under vigorous stirring. Stirring was stopped after 10 s, and the seeds were left undisturbed at 30 °C for 1 h. Afterward, 190 μL of HCl 1 M and 100 μL of $HAuCl_4$ 50 mM solution were added to 10 mL of CTAB 0.1 M, and the mixture was stirred for 5 min. Subsequently, 120 μL of $AgNO_3$ 0.01 M solution was added to the mixture under moderate stirring, followed by 80 μL of 0.1 M ascorbic acid, which turned the solution colorless within seconds. Finally, 24 μL of the previous seeds were added, stirred for 10 s, and left undisturbed at 30 °C for 2 h. AuNRd were centrifuged and redispersed in water to remove the excess of surfactant.
3. Au Nanostars (NSt) were obtained via a seed-mediated growth method.[29] The previous citrate-stabilized AuNSp were used as seeds. To prepare the growth solution, HCl (10 μL, 1 M) was added to a $HAuCl_4$ solution (10 mL, 0.25 mM). Then, 100 μL of seed solution (0.5 mM) was added, followed by ascorbic acid (50 μL, 0.1 M) and $AgNO_3$ (100 μL, 3 mM), under stirring. Finally, CTAB was added (0.2 mL, 0.1M). After 30 min of incubation, AuNSt were ready for use.
4. PBA-NiFe NPs were synthesized by adding simultaneously two aqueous solutions: (i) 40 mL of $NiCl_2{\cdot}6H_2O$ (10 mM) and (ii) 40 mL of $K_3[Fe(CN)_6]$ (10 mM) and CsCl (50 mM). Then, the mixtures were stirred for half an hour before being centrifuged at 11,000 rpm for 20 min. The final solution was centrifuged at 13,000 rpm for 15 min thrice (in water).

2.3. Synthesis of Core@Shell NPs.

1. AuNSp@PBA: 10 μL of 1 mM 4-MPy was added to 10 mL of Au NSp (concentration of 0.5 mM), and the solution was stirred for 20 min to allow the 4-MPy to interact with the surface of Au NSp. Then, the solution was centrifuged (8000 rpm, 20 min) for the removal of the excess citrate and 4-MPy, and redispersed in 10 mL of ultrapure water. For the growth of the PBA shell, the following precursor solutions were prepared: (i) 10 mM of $NiCl_2$, and (ii) 10 mM of $K_3[Fe(CN)_6]$ and 50 mM of CsCl. A total of 100 μL of each solution was added simultaneously into the colloidal Au@4-MPy NPs under 1200 rpm stirring and at an addition rate of 10 μL per 20 s. The final solution was left to stir for 20 min and centrifuged at 13,000 rpm for 15 min thrice (in water).
2. AuNRd@PBA: 1 mL of 1 mM aqueous solution of 4-MPy was added to 4.5 mL of the previous AuNRd solution to functionalize the Au surface. After 20 min of stirring, the resulting solution was centrifuged at 8000 rpm for 30 min and redispersed in 10 mL of water. For the growth of the PBA shell, the following precursor solutions were used: (i) 5 mM of $NiCl_2$ and (ii) 5 mM of $K_3[Fe(CN)_6]$ and 25 mM of CsCl. A total of 100 μL of each solution was added simultaneously into the colloidal Au@4-MPy NPs under 1200 rpm stirring and at an addition rate of 10 μL per 20 s. The final solution was left to stir for 20 min and centrifuged at 8000 rpm for 30 min thrice (in water).
3. AuNSt@PBA: 1 mL of 1 mM 4-MPy was added to 4.5 mL of the previous AuNSt solution to functionalize the Au surface. After 20 min of stirring, the resulting solution was centrifuged at 3000 rpm for 30 min to remove the excess CTAB and 4-MPy, and it was redispersed in 10 mL of Milli-Q water. For the growth of the PBA shell, the following precursor solutions were used: (i) 5 mM of $NiCl_2$ and (ii) 5 mM of $K_3[Fe(CN)_6]$ and 25 mM of CsCl. A total of 100 μL of each solution was added into the colloidal Au@4-MPy NPs under 1200 rpm stirring and at an addition rate of 10 μL per 20 s. The final solution was left to stir for 20 min and centrifuged at 3000 rpm for 30 min thrice (in water).

The estimated hazards of the synthesized NPs are low, based on those of closely related known analogues.

2.4. Physical Characterization. The UV−vis absorption spectra were recorded on a Thermofischer multiskan skyhigh microplate spectrophotometer from 300 to 900 nm range. Transmission electron microscopy (TEM): TEM studies were carried out on a Jeol 300 arm microscope operating at 80 kV and a Technai G2 F20 microscope operating at 200 kV. Samples were prepared by dropping suspensions on lacey Formvar/carbon copper grids (300 mesh). Zeta potential (ZP) and dynamic light scattering (DLS) were performed with a Zetasizer Nano ZS instrument (Malvern Instruments Ltd.). Attenuated total reflectance Fourier-transform infrared (ATR-FTIR): spectra were collected in an Agilent Cary 630 FTIR spectrometer in the 4000−500 cm^{-1} range. Magnetic measurements: Magnetic data were collected with a Quantum Design MPMS XL-5 susceptometer. DC FC magnetization measurements were performed under an applied magnetic field of 100 Oe. The isothermal magnetization at 2 K was performed between −7 and +7 T. The diamagnetic contributions were corrected using the Pascal tables, taking into account the molecular formula of the heterostructures extracted from EDX. The following masses were weighted for PBA, AuNSp@PBA, AuNRd@PBA, and AuNSt@PBA samples: 2.15, 0.40, 0.05, and 0.15 mg. Power X-ray Diffraction (PXRD) patterns were collected in a PANalytical Empyrean diffractometer using copper radiation (Cu K α λ= 1.5418 Å) with a PIXcel detector, operating at 40 mA and 45 kV at room temperature. X-ray Photoelectron Spectroscopy (XPS) measurements were done with a KALPHA

https://doi.org/10.1021/acs.inorgchem.4c05320
Inorg. Chem. 2025, 64, 6510−6518

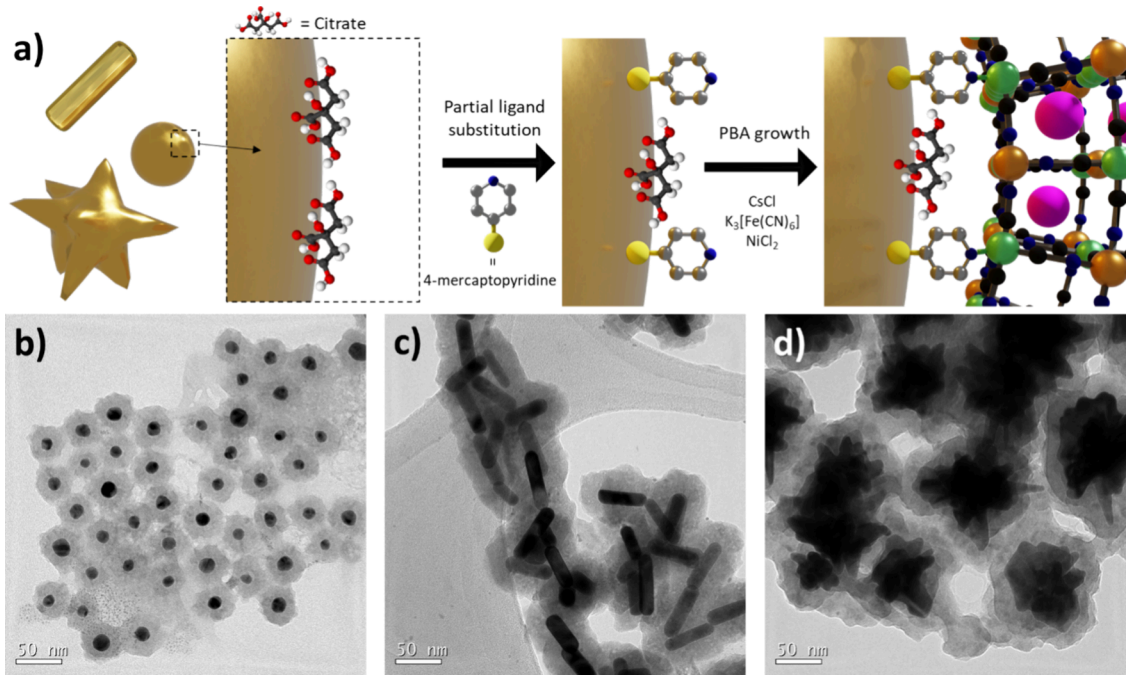

Figure 1. (a) Schematic illustration of the developed method for the preparation of Au@PBA NPs. TEM images of the obtained core@shell NPs using as core: (b) spheres (NSp), (c) rods (NRd), and (d) stars (NSt).

Thermo Scientific spectrometer. All spectra were collected using Al Kα radiation (1486.6 eV) and monochromated by a twin crystal monochromator, yielding a focused X-ray spot (elliptical in shape with a major axis length of 200 μm) at 30 mA and 2 kV. The alpha hemispherical analyzer was operated in the constant energy mode with a survey scan pass energy of 200 eV to measure the whole energy band and 50 eV in a narrow scan to selectively measure the particular elements. XPS data were analyzed with the Avantage software. A background function was used to approximate the experimental backgrounds. Charge compensation was achieved with the system flood gun that provides low-energy electrons and low-energy argon ions from a single source. For the electrochemical characterization, a dispersion composed of 1 mg of powder material, 0.5 mg of acetylene black, 200 μL of water and ethanol (1:1), and 8 μL of Nafion (10%) was sonicated in order to obtain a well-dispersed suspension. Then, 5 μL was drop-cast in a previously polished (with 0.05 μm alumina powder) 3 mm Ø Glassy Carbon electrode. Afterward, the solvent was evaporated at room temperature. The electrode PBA mass loading achieved was around 0.34 mg·cm^{-2}. Electrochemical tests were performed in a three-electrode cell equipped with a Rotating Disk Electrode Glassy Carbon acting as the working electrode and with a platinum foil and a silver−silver chloride (Ag/AgCl (3 M KCl)) as the counter electrode and reference electrode, respectively. All potentials were converted by referring to the reversible or the normal hydrogen electrode (RHE and NHE). The measurements were performed at least two times for every sample using different electrodes on an Autolab PGSTAT 128N potentiostat/galvanostat. Linear sweep voltammetry (LSV) measurements were carried out at 5 mV·s^{-1} and at 1600 rpm in a previously Ar purged sodium phosphate (0.1 M) aqueous solution at pH 6.9 containing $NaNO_3$ (1M) as the electrolyte. The first LSV is shown. Subsequent cycles did not show significant variation. Prior to this, cyclic voltammetry (CVs) measurements were performed at different scan rates to activate the electrocatalysts. The concentration of redox active Ni centers was estimated from the slope of the linear relationship between the peak current of the oxidation wave and the scan rate.[30] Electrochemical impedance spectroscopy (EIS) measurements were carried out using a Gamry 1010E potentiostat/galvanostat controlled by Gamry software by applying an AC amplitude of 10 mV in the frequency range 10^0−10^5 Hz at an overpotential of 0.9 V. EIS data were analyzed and fitted by means of Gamry Echem Analyst v. 7.07 software.

3. RESULTS AND DISCUSSION

To obtain Au@PBA NPs with different shapes (spheres, rods, and stars), we developed a two-step protocol that involves introducing an anchoring molecule on the Au surface to facilitate the growth of a PBA shell while minimizing Au etching by the cyanide species (Figure 1a). To achieve this, a 4-MPy molecule was used to partially functionalize the Au surface. 4-MPy was chosen in accordance with previous works dedicated to the growth of cyanide-based coordination polymers on 4-MPy self-assembled monolayers on gold.[25,31] In this way, the presence of N in the para-position with respect to the thiol group can facilitate the alignment between the core and shell. Note that to ensure the colloidal stability of the NPs, which is essential for growing the PBA shell, we performed a partial functionalization. This is a key step because 4-MPy alone cannot efficiently stabilize the different Au NPs in solution. This is evidenced by the broadening of the plasmonic peaks of the different nanoforms or the appearance of additional peaks, indicating aggregation upon the successive addition of 4-MPy (Figure S1).[32]

As demonstrated by attenuated total reflectance Fourier transform infrared spectroscopy (ATR-FTIR), the initial capping agents (citrate for the Au NSp, CTAB for the NRd and NSt) remain present in the nanoforms with the maximum amount of 4-MPy added without compromising their colloidal stability (Figure S2). On the other hand, the presence of 4-MPy was confirmed by high-resolution X-ray photoelectron spectroscopy (XPS) in the S 2p region, due to the sulfur atom of 4-MPy (Figure S3). Specifically, in the S 2p region, 4-MPy-functionalized nanoforms display sulfur bands, with the main S 2p3/2 peak at approximately 162.3 eV, which is consistent with the expected signal of sulfur bound to Au, similar to that observed in self-assembled monolayers of 4-MPy on gold

https://doi.org/10.1021/acs.inorgchem.4c05320
Inorg. Chem. 2025, 64, 6510−6518

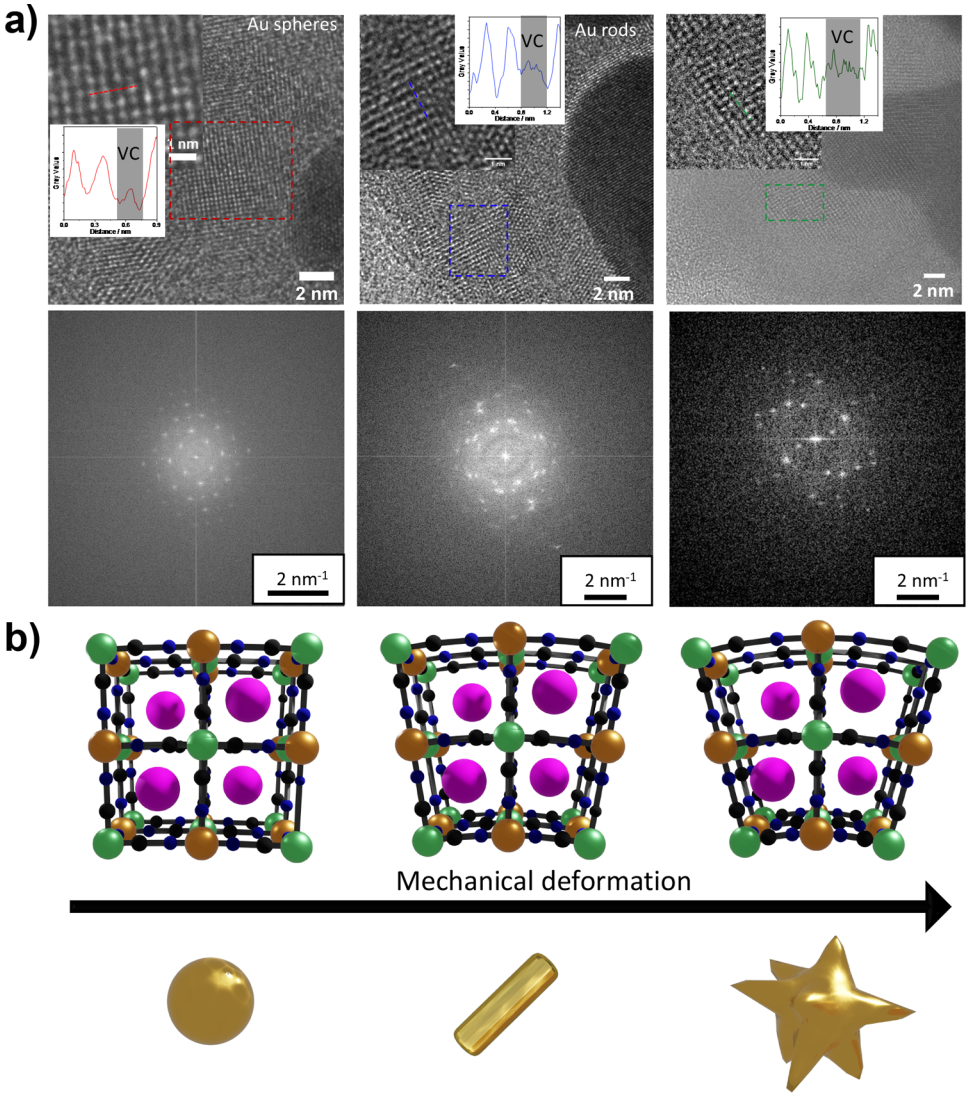

Figure 2. (a) HRTEM image of the AuNSp@PBA (top left), AuNRd@PBA (top center), and AuNSt@PBA (top right). Insets show a magnification of the shell, showing the Ni−Fe classical pattern with Fe-CN vacancies. Below it is depicted the FTT at the interface (the marked region with discontinuous dots) of the same images for the AuNSp@PBA (middle left), AuNRd@PBA (middle center), and AuNSt@PBA (middle right). (b) Scheme of the strain that may be sensed by $CsNi[Fe(CN)_6]$ at the Au/PBA interface depending on the Au morphology.

substrates (for more information, see the SI, Figure S3). This indicates that the functionalization mainly occurs by the formation of Au−S chemical bonds, thanks to the strong affinity of thiols for metallic Au.[33]

In the case of spherical Au NPs, we found that an optimal 4-MPy:Au molar ratio of 0.002 provides the highest number of anchoring molecules on the Au surface while preserving colloidal stability (Figure S4). Attempts to quantify the amount of anchored 4-MPy by using thermogravimetric analysis (TGA) were unsuccessful. This is because both citrate-stabilized and 4-MPy-functionalized Au NPs show only a gradual and subtle mass loss (Figure S5), making precise quantification impossible. This limitation arises from the small amounts of citrate and 4-MPy relative to the large bulk mass of Au NPs as well as the significant weight of individual Au atoms. Additionally, strong Au-molecule interactions likely cause gradual decomposition rather than the sharp transitions typically observed in functionalized inorganic systems.[34] For rod- and star-shaped Au NPs stabilized with CTAB, a 4-MPy:Au molar ratio 100 times higher was required. To quantify the amount of 4-MPy on their surfaces, we carried out XPS analysis of the N 1s region, comparing nitrogen from CTAB (N-CTAB) and 4-MPy (N-MPy). After functionalization, a new band at 400 nm appears (Figure S6), confirming the 4-MPy attachment. Based on the nitrogen ratio, we estimate that 30% of the AuNRd surface and 20% of the AuNSt surface are functionalized with 4-MPy.

The final step of the procedure involves the simultaneous addition of the PBA precursors ($NiCl_2$ $6H_2O$, CsCl and $K_3Fe(CN)_6$) to the colloidal solution containing 4-MPy-modified Au NPs (Figure 1a). $Ni^{II}Fe^{III}$−PBA was prepared because it is one of the few PBAs that exhibit a pure ferromagnetic response[35,36] and due to its excellent OER catalytic properties.[8] Cs was selected as the countercation because its ionic radius (1.8 Å) closely matches the interstitial site within PBA,[37] and thus, no additional distortion beyond that produced by the Au core is expected. In terms of shell formation, thanks to the presence of the N atom from the pyridine, there are two possible anchoring points for the PBA, the pyridine for the Ni^{II} ions and the ferrocyanide that can

https://doi.org/10.1021/acs.inorgchem.4c05320
Inorg. Chem. 2025, 64, 6510−6518

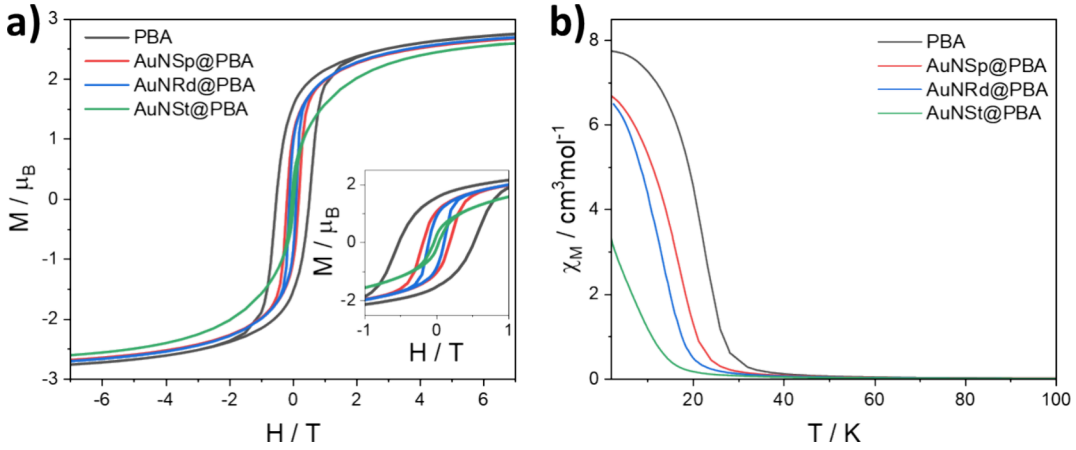

Figure 3. (a) Isothermal magnetization at 2K of bare PBA, AuNSp@PBA, AuNRd@PBA, and AuNSt@PBA. (b) Thermal magnetic susceptibility of the same NPs.

interact with the gold through the CN^-. The interaction of both ions with the Au surface was explored independently by adding only one of the two ions on 4-MPy-functionalized Au NSp. The presence of Ni^{II} (or $[Fe(CN)_6]^{3-}$) ions was confirmed by XPS by looking at the Ni 2p (or Fe 2p) regions (Figure S7c). However, it must be noted that adding only ferrocyanide causes gold surface etching mediated by the CN^- groups (Figure S8). This is evidenced by the drop in sulfur content in the S 2p region, which corresponds to 4-MPy molecules anchored at the NPs surface (Figure S7b). Therefore, 4-MPy is especially useful when forming PBA shells around gold cores, as it provides extra anchoring points for shell growth while protecting the gold core from etching.

During the synthesis, a noticeable color change in the solution occurs during shell formation (Figure S9). This change is a consequence of the sensitivity of the plasmon band to the alterations in the refractive index around the Au surface, from 1.33 (water) to 1.56 (PBA),[38−40] and thus, it indicates the existence of an interaction between Au and PBA. Notably, the plasmonic shifts for rods and stars are, as expected, more pronounced than for the spheres (Table S1), due to the higher optical sensibility of these anisotropic structures at the tips (hot spots).[39,41]

After completing the addition, we evaluated the size distribution and colloidal stability of the core@shell nanoparticles using dynamic light scattering (DLS). The DLS results showed a narrow size distribution in water, with hydrodynamic diameters of 47 ± 20, 147 ± 38, and 130 ± 30 nm for spheres, rods, and stars, respectively (Figure S10). Remarkably, no significant aggregation was observed as secondary peaks in DLS. This was further confirmed by Z-potential analysis (Table S2), which shows values around −36, −23, and −20 mV for spheres, rods, and stars, respectively, supporting the excellent colloidal stability of the core@shells. Note that for the anisotropic NPs, Z-potential values undergo a significant shift from positive to negative after the PBA overgrowth. 4-MPy functionalization reduces the positive charge on the NP surface (to about 0 mV), preventing charge reversal, which can result in aggregation during shell formation.

Through transmission electron microscopy (TEM), we could observe the formation of a clear core@shell structure in all cases, with a well-formed PBA shell (ca. 15 nm) rather than a composite made of gold and PBA (Figures 1b−d, S11, and S12). In this line, energy-dispersive X-ray spectroscopy (EDX, Figure S12) mappings evidence the presence of Ni and Fe in the shell, while the gold is confined in the core, regardless of the nanoarchitecture of the core. On the contrary, without the prior addition of 4-MPy, the PBA tends to self-nucleate as independent NPs rather than coating on the Au surface (Figure S13), pointing out the importance of the MPy for the proper formation of the PBA shell. In addition, the molecular formulas estimated by EDX for the PBA shells show a comparable Cs:Ni:Fe ratio of 1.12−2.12:0.53−0.69:0.84−0.86 (see Table S3), suggesting the formation of the same PBA with some iron vacancies.

Next, the different PBA shells were characterized and compared to the pristine PBA by means of different techniques, including ATR-FTIR, XPS, and powder X-ray diffraction (PXRD). The same vibrational modes and Fe 2p and Ni 2p features were seen for the core@shell nanostructures and bare PBA (Figures S14 and S15). This resemblance indicates the formation of the expected PBA in all cases. Furthermore, although the same structure was observed in all samples, a subtle shift to higher angles was noticed in PXRD for the PBAs overgrown around gold (Figure S16a,b), which could be attributed to some structural distortions causing a decrease in the Ni to Fe distance. The Williamson−Hall plot of the XRD patterns indicates that the PBA in the heterostructures has a smaller crystalline size compared to bare PBA, and this polycrystallinity increases with the anisotropy of the gold core (see SI, Figure S12c). Similarly, Williamson−Hall analysis also suggests that the PBA lattice strain increases when grown around gold cores, in particular, in the anisotropic heterostructures (NRd and NSt). To further understand this effect, we conducted a detailed analysis of the shell crystallographic structure at the Au/PBA interface by high-resolution transmission electron microscopy (HR-TEM). As shown in Figure 2, all the PBA shells display a remarkable crystallinity, exhibiting in all the heterostructures the expected coherent shepherd-check pattern related to the alternating Ni and Fe atomic array. In this way, the Ni−Fe distances within the cubic lattice can be calculated by filtering the most crystalline areas of the different shells (Figures S17−Insets S22), obtaining values of around 5.1 Å in all cases, which is consistent with the expected Ni−NC−Fe distance.[42] Moreover, the lattice discontinuity supports the presence of Fe-CN vacancies, which can be directly monitored from the HR-TEM images, Insets Figure 2.

https://doi.org/10.1021/acs.inorgchem.4c05320
Inorg. Chem. 2025, 64, 6510−6518

The polycrystallinity and strain clearly modify the PBA magnetic response, as observed by SQUID magnetometry (Figure 3). In this line, isothermal magnetization curves recorded at 2 K (Figure 3a) show a magnetic saturation close to 3 μB at 7T for the bare NPs and all the core@shell nanostructures, confirming the main oxidation state of the PBA shell as Ni^{II} and Fe^{III}. This value corresponds to a total spin S = 1.5, matching the S_{NiFe} of the ferromagnetic interaction of Ni^{II} (S_{Ni} = 1) and Fe^{III} (S_{Fe} = 1/2). The discrepancy from the ideal value is likely due to the presence of some minor Ni^{II}−Fe^{II} PBA species. Nevertheless, a significant decrease in the coercive field of the core@shells with respect to the bare PBA can also be also noticed. This suggests that the magnetic cooperativity of PBA is affected in the core@shell configuration, as indicated by the decreasing coercive field with increasing core anisotropy (see Table S5). A similar conclusion can be extracted from the temperature-dependent magnetic susceptibility (Figure 3b). When decreasing the temperature, a rise in the magnetic response of all of the NPs can be noticed, which is attributed to the PBA ferromagnetism. This increase is abrupt for all the nanostructures except for the AuNSt@PBA. Furthermore, the Curie temperature (T_c) of the PBA shifts to lower temperatures as the anisotropy of the core increases (Figure 3b), particularly for the stars.

It is worth mentioning that for the AuNSt@PBA, the magnetic remanence and Tc are lower than in the PBA. We attributed this effect to two main reasons: (1) As evidenced by the lower value of Magnetic saturation at 7T (2.6 μB) to a larger presence of reduced Ni^{II}−Fe^{II} species compared to the other heterostructures, which can produce a reduction in the Tc.[37,43] (2) The presence of two types of PBAs with different magnetic behaviors: one in close contact with the Au surface and another located farther from the core. To corroborate this, we additionally prepared AuNSt@PBA heterostructures with a thinner shell (below 10 nm) and a thicker shell (above 20 nm), and we compared the magnetic properties of the three samples. As expected, we observed an almost entirely paramagnetic response from the heterostructure with the thinnest shell, while the thickest shell exhibited a behavior nearly identical to that of bulk PBA (see SI, Figure S23). This is in good agreement with the aforementioned electron diffraction experiments, which showed that the influence of the core anisotropy on the PBA crystalline structure decreases beyond 10 nm from the Au surface. Therefore, it is reasonable to assume that for shells below 10 nm thickness, the Ni and Fe species are weakly coupled due to the larger polycrystallinity and structural deformation,[44] resulting in a paramagnetic response. In contrast, the species farther from the Au surface exhibit the characteristic ferromagnetic response of the strongly coupled Ni-NC-Fe species.

After characterizing the different PBA shells, we explored their performance as OER electrocatalysts, considering the potential positive effects of strain and the smaller crystallite size on water-splitting electrocatalysis. Strain in the PBA structure can modify electronic properties by increasing the density of active sites, thereby enhancing the water-splitting reaction.[45,46] Additionally, smaller crystallite sizes expose more surface sites, particularly at edges where catalysis is most active, leading to a higher density of catalytic sites and improved charge transport, further boosting overall electrocatalytic performance.[47]

To evaluate these effects, in the first step, cyclic voltammetries (CVs) were performed to activate the materials and estimate the amount of electroactive Ni species (Figure S24). Since the samples may exhibit different electrochemical surface areas due to their different crystalline domain sizes, the electrochemical performance was normalized to the number of electroactive species with the aim of investigating the intrinsic catalytic activity of the PBA sites. Subsequently, their OER electrochemical activity was tested and compared by linear sweep voltammetry (LSV) performed at a slow scan rate (5 mV s^{-1}) in order to minimize capacitive currents (Figure 4a; raw data can be found in Figure S25). To analyze the different OER performances exhibited by the materials, the current densities at a potential of 2.04 V versus RHE (Figure 4b) and Tafel slopes (Figure 4c) were compared. Note that although some coordination polymers can undergo surface conversion into hydroxides/oxides,[48] the PBA shell remains unaffected after these measurements due to its high stability at neutral pH (Figures S26 and S27).

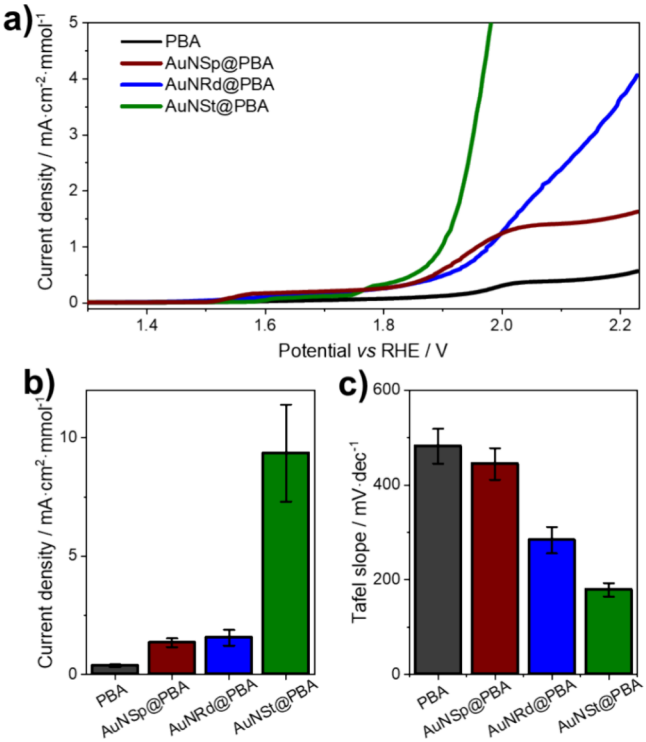

Figure 4. (a) Linear sweep voltammetry of the different samples recorded at 5 mV s^{-1} in NaP_i (0.1 M) buffer solution at pH 6.9 with $NaNO_3$ (1 M) as the electrolyte. Current density values were normalized to the number of electroactive species. (b) Current densities obtained at a potential of 2.04 V vs RHE (an overpotential of 800 mV vs OER). (c) Tafel slopes calculated from LSV data.

The results evidence that the presence of a Au core enhances the performance of the PBA. For example, the current density is increased from 0.37 to 1.34 mA cm^{-2} $mmol^{-1}$ (ca. 360% improvement), while the Tafel slope is slightly decreased by 38 mV dec^{-1} when a spherical Au core is introduced. As previously reported, the presence of an Au core can modify the electronic structure of Co, Ni, and Fe sites, stabilizing their oxidized electroactive species, improving the conductivity of the shell material, and thus enhancing OER performance.[15] Interestingly, the displayed OER performance of the different Au@PBA NPs varies depending on the core shape. Given that the obtained PBA nanostructures have a similar composition and their activity is normalized to the electroactive species, this

https://doi.org/10.1021/acs.inorgchem.4c05320
Inorg. Chem. 2025, 64, 6510−6518

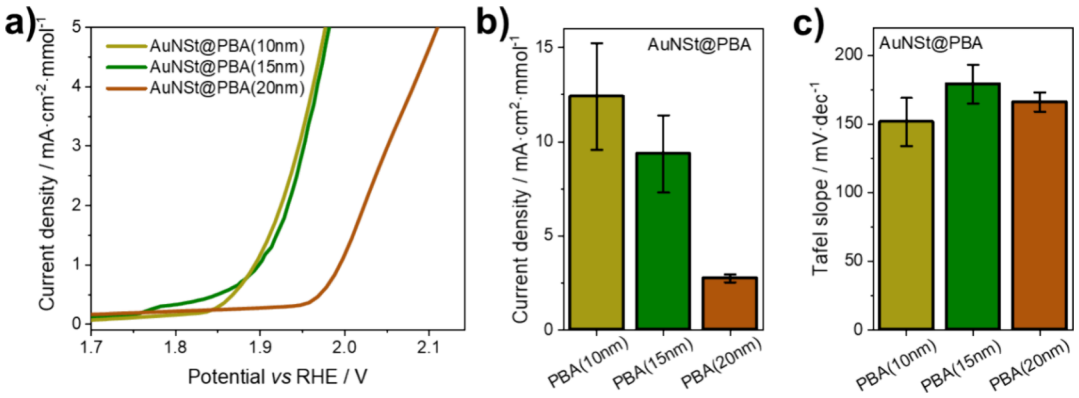

Figure 5. (a) Linear sweep voltammetry of the AuNSt@PBA with different PBA shell thicknesses recorded at 5 mV s^{-1} in NaPi (0.1 M) buffer solution at pH 6.9 with $NaNO_3$ (1 M) as the electrolyte. Current density values were normalized to the number of electroactive species (Figures S29 and S30). (b) Current densities obtained at a potential of 2.04 V vs RHE (an overpotential of 800 mV vs OER). (c) Tafel slopes calculated from LSV data.

variation in the OER can be attributed to the presence of strain and multiple crystallographic domains. In this regard, it can be noticed that the anisotropic NPs exhibit better performance than the spherical heterostructure, and their efficiency improves with higher strain and polycrystallinity. For the star-shaped NPs, the current density at a potential of 2.04 V is increased by ca. 690 and 600%, while the kinetics values are reduced by around 260 and 100 mV dec^{-1} with respect to the spheres and rods, respectively. To understand this improvement, the OER kinetics of the heterostructures were analyzed by means of Electrochemical Impedance Spectroscopy (Figure S28). In particular, their internal and OER resistances were examined (see SI for more information) due to their importance in the catalytic process. On the one hand, the presence of a gold core produces a noteworthy reduction in the internal resistance (R_{int}) due to the higher conductivity, but the R_{int} does not significantly vary with the core shape. On the other hand, the resistance related to OER (R_{OER}) decreases when gold is incorporated, and it decreases even more as gold anisotropy increases. This reduction in R_{OER} is attributed to the PBA reactivity that becomes higher with strain and polycrystallinity.

Lastly, we evaluated the impact of the shell thickness on the catalytic activity by studying the performance of the most active heterostructure (AuNSt@PBA) exhibiting different shell thicknesses: below 10 nm, around 15 nm, and above 20 nm. As shown in Figure 5, NPs with less than a 10 nm shell perform similarly to those with 15 nm. This can be attributed to the intrinsic porosity of PBAs, which facilitates ion diffusion, allowing catalytic activity to extend beyond the outer surface into the inner structure, accessing internal active sites.[49] However, when the shell thickness exceeds 20 nm, the NPs exhibit a lower catalytic activity than those with thinner shells likely due to reduced accessibility to strained active sites.

4. CONCLUSIONS

In this work, we have developed a general protocol for synthesizing core@shell NPs formed by a magnetic CsNi[Fe-$(CN)_6$] PBA shell wrapping individual Au NPs with different morphologies (spheres, rods, and stars). Our method relies on functionalizing Au with 4-mercaptopyridine, providing an extra anchoring site for the subsequent PBA growth. This approach offers several key advantages: first, it protects Au from cyanide-induced etching, enabling the use of anisotropic Au NPs as the core; second, it enables PBA growth without the inclusion of a reducing agent, allowing for the synthesis of nonreduced PBA shells based on Fe^{III} ions, thus putting in direct contact the Au core with the ferromagnetic shell. Therefore, this system is ideal for many applications due to the expected synergy between the properties of the metallic core and the magnetism of the PBA shell.

Furthermore, we observed that the curvature of the Au cores leads to a polycrystalline shell featuring significant strain, which is directly correlated to the NP shape. By means of HR-TEM, we detected at the Au/PBA interface multiple crystallographic domains and a compressive strain of 1.2, 1.5, and 2% for the PBA grown around Au nanospheres, nanorods, and nanostars, respectively. Both effects enhance the electrochemical performance of PBA as an OER catalyst. Particularly, when utilizing star-shaped cores (the most anisotropic heterostructures), we observe remarkable improvements in both the onset potential and Tafel slope compared to the pristine PBA materials, showcasing nearly a 10-fold enhancement in the intrinsic electrocatalytic activity. Thus, our work paves the way for creating novel Au@PBA nanostructures with exciting new synergistic effects and enhanced properties induced by anisotropic cores.

■ ASSOCIATED CONTENT

Supporting Information

The Supporting Information is available free of charge at https://pubs.acs.org/doi/10.1021/acs.inorgchem.4c05320.

X-ray diffraction, infrared spectra, UV−vis spectra, TEM images, TGA measurements, EDX measurements, magnetic measurements, DLS and Zeta Potential measurements, XPS spectra, and additional electrochemical characterization (PDF)

■ AUTHOR INFORMATION

Corresponding Authors

Ramón Torres-Cavanillas − *Instituto de Ciencia Molecular, Universitat de València, 46980 Paterna, Spain; Department of Materials, University of Oxford, Oxford OX2 6NN, U.K.*; Email: ramon.torres@uv.es

Roger Sanchis-Gual − *Instituto de Ciencia Molecular, Universitat de València, 46980 Paterna, Spain*; Email: roger.sanchis@uv.es

https://doi.org/10.1021/acs.inorgchem.4c05320
Inorg. Chem. 2025, 64, 6510−6518

Eugenio Coronado − *Instituto de Ciencia Molecular, Universitat de València, 46980 Paterna, Spain;* orcid.org/0000-0002-1848-8791; Email: eugenio.coronado@uv.es

Authors

Shoaib Azeem − *Instituto de Ciencia Molecular, Universitat de València, 46980 Paterna, Spain;* orcid.org/0000-0003-1523-8700

Joaquín Soriano-López − *Instituto de Ciencia Molecular, Universitat de València, 46980 Paterna, Spain;* orcid.org/0000-0002-9203-3752

Isaac Brotons-Alcázar − *Instituto de Ciencia Molecular, Universitat de València, 46980 Paterna, Spain;* orcid.org/0000-0002-1787-3348

Christopher Allen − *Electron Physical Science Imaging Centre, Diamond Light Source, Didcot OX11 0DE, U.K.*

Complete contact information is available at: https://pubs.acs.org/10.1021/acs.inorgchem.4c05320

Author Contributions

The manuscript was written through contributions of all authors. All authors have given approval to the final version of the manuscript.

Notes

The authors declare no competing financial interest.

■ ACKNOWLEDGMENTS

The authors acknowledge funding from the EU (ERC AdG Mol-2D 788222, FET OPEN SINFONIA 964396, and Pathfinder-4D-NMR 101099676), the Spanish MCIU (Unit of Excellence "Maria de Maeztu" CEX2019-000919-M, Project COMCUANTICA/010, 2D-SPICE PID2023-149309OB-I00 and Project IDIFEDER/2021/078 cofinanced by FEDER), and the Generalitat Valenciana (Prometeo Programme PROMETEO/2021/022). R.S.-G. thanks the Spanish Ministry of Universities and the European Union for a "Margarita Salas" postdoctoral fellowship (Next Generation EU). R.T.-C. thanks the Generalitat Valenciana for his APOSTD Fellowship (CIAPOS/2021/269). J.S.-L. acknowledges the funding from Generalitat Valenciana thought the Plan Gen-T of Excellence (CDEIGENT/2021/037). The electron microscopy experiments were performed on the ePSIC at Diamond Synchrotron, United Kingdom (proposal number MG35687). The authors congratulate Professor Marius Andruch on his 70th anniversary.

■ REFERENCES

(1) Torres-Cavanillas, R.; Morant-Giner, M.; Escorcia-Ariza, G.; Dugay, J.; Canet-Ferrer, J.; Tatay, S.; Cardona-Serra, S.; Giménez-Marqués, M.; Galbiati, M.; Forment-Aliaga, A.; Coronado, E. Spin-Crossover Nanoparticles Anchored on MoS2 Layers for Heterostructures with Tunable Strain Driven by Thermal or Light-Induced Spin Switching. *Nat. Chem.* **2021**, *13* (11), 1101−1109.

(2) Morant-Giner, M.; Sanchis-Gual, R.; Romero, J.; Alberola, A.; García-Cruz, L.; Agouram, S.; Galbiati, M.; Padial, N. M.; Waerenborgh, J. C.; Martí-Gastaldo, C.; Tatay, S.; Forment-Aliaga, A.; Coronado, E. Prussian Blue@MoS2Layer Composites as Highly Efficient Cathodes for Sodium- and Potassium-Ion Batteries. *Adv. Funct. Mater.* **2018**, *28*, No. 1706125.

(3) Guari, Y.; Cahu, M.; Félix, G.; Sene, S.; Long, J.; Chopineau, J.; Devoisselle, J.; Larionova, J. Nanoheterostructures Based on Nanosized Prussian Blue and Its Analogues: Design, Properties and Applications. *Coord. Chem. Rev.* **2022**, *461*, No. 214497.

(4) Sanchis-Gual, R.; Coronado-Puchau, M.; Mallah, T.; Coronado, E. Hybrid Nanostructures Based on Gold Nanoparticles and Functional Coordination Polymers: Chemistry, Physics and Applications in Biomedicine, Catalysis and Magnetism. *Coord. Chem. Rev.* **2023**, *480*, No. 215025.

(5) Hu, P.; Morabito, J. V.; Tsung, C. K. Core-Shell Catalysts of Metal Nanoparticle Core and Metal-Organic Framework Shell. *ACS Catal.* **2014**, *4* (12), 4409−4419.

(6) Felts, A. C.; Andrus, M. J.; Knowles, E. S.; Quintero, P. A.; Ahir, A. R.; Risset, O. N.; Li, C. H.; Maurin, I.; Halder, G. J.; Abboud, K. A.; Meisel, M. W.; Talham, D. R. Evidence for Interface-Induced Strain and Its Influence on Photomagnetism in Prussian Blue Analogue Core-Shell Heterostructures, RbaCob[Fe(CN)6]c??MH2O@KjNik-[Cr(CN)6]l??NH2O. *J. Phys. Chem. C* **2016**, *120* (10), 5420−5429.

(7) Catala, L.; Mallah, T. Nanoparticles of Prussian Blue Analogs and Related Coordination Polymers: From Information Storage to Biomedical Applications. *Coord. Chem. Rev.* **2017**, *346*, 32−61.

(8) Cao, L. M.; Lu, D.; Zhong, D. C.; Lu, T. B. Prussian Blue Analogues and Their Derived Nanomaterials for Electrocatalytic Water Splitting. *Coord. Chem. Rev.* **2020**, *407*, No. 213156.

(9) Huang, Y.; Ren, S. Multifunctional Prussian Blue Analogue Magnets: Emerging Opportunities. *Appl. Mater. Today* **2021**, *22*, No. 100886.

(10) Fétiveau, L.; Paul, G.; Nicolas-Boluda, A.; Volatron, J.; George, R.; Laurent, S.; Muller, R.; Sancey, L.; Mejanelle, P.; Gloter, A.; Gazeau, F.; Catala, L. Tailored Ultra-Small Prussian Blue-Based Nanoparticles for MRI Imaging and Combined Photothermal/Photoacoustic Theranostics. *Chem. Commun.* **2019**, *55* (98), 14844−14847.

(11) Sato, O.; Iyoda, T.; Fujishima, A.; Hashimoto, K. Photoinduced Magnetization of a Cobalt-Iron Cyanide. *Science.* **1996**, *272* (5262), 704−705.

(12) Ohkoshi, S.; Arai, K.-I.; Sato, Y.; Hashimoto, K. Humidity-Induced Magnetization and Magnetic Pole Inversion in a Cyano-Bridged Metal Assembly. *Nat. Mater.* **2004**, *3* (12), 857−861.

(13) Han, L.; Tang, P.; Reyes-Carmona, Á.; Rodríguez-García, B.; Torréns, M.; Morante, J. R.; Arbiol, J.; Galan-Mascaros, J. R. Enhanced Activity and Acid PH Stability of Prussian Blue-Type Oxygen Evolution Electrocatalysts Processed by Chemical Etching. *J. Am. Chem. Soc.* **2016**, *138* (49), 16037−16045.

(14) Itaya, K.; Shoji, N.; Uchida, I. Catalysis of the Reduction of Molecular Oxygen to Water at Prussian Blue Modified Electrodes. *J. Am. Chem. Soc.* **1984**, *106* (12), 3423−3429.

(15) Sanchis-Gual, R.; Otero, T. F.; Coronado-Puchau, M.; Coronado, E. Enhancing the Electrocatalytic Activity and Stability of Prussian Blue Analogues by Increasing Their Electroactive Sites through the Introduction of Au Nanoparticles. *Nanoscale* **2021**, *13* (29), 12676−12686.

(16) Zhang, M.; Zhang, W.; Engelbrekt, C.; Hou, C.; Zhu, N.; Chi, Q. Size-Dependent and Self-Catalytic Gold@Prussian Blue Nanoparticles for the Electrochemical Detection of Hydrogen Peroxide. *ChemElectroChem.* **2020**, *7* (18), 3818−3823.

(17) Su, Y. Y.; Jiang, X. Y.; Zheng, L. J.; Yang, Y. W.; Yan, S. Y.; Tian, Y.; Tian, W.; Liu, W. F.; Teng, Z. G.; Yao, H.; Wang, S. J.; Zhang, L. J. Hybrid Au-Star@Prussian Blue for High-Performance towards Bimodal Imaging and Photothermal Treatment. *J. Colloid Interface Sci.* **2023**, *634*, 601−609.

(18) Jing, L.; Liang, X.; Deng, Z.; Feng, S.; Li, X.; Huang, M.; et al. Biomaterials Prussian Blue Coated Gold Nanoparticles for Simultaneous Photoacoustic/CT Bimodal Imaging and Photothermal Ablation of Cancer. *Biomaterials* **2014**, *35* (22), 5814−5821.

(19) Shen, Y. M.; Gao, M. Y.; Chen, X.; Shen, A. G.; Hu, J. M. Fine Synthesis of Prussian-Blue Analogue Coated Gold Nanoparticles (Au@PBA NPs) for Sorting Specific Cancer Cell Subtypes. *Spectrochim. Acta - Part A Mol. Biomol. Spectrosc.* **2021**, *252*, No. 119566.

(20) Jana, N. R.; Gearheart, L.; Obare, S. O.; Murphy, C. J. Anisotropic Chemical Reactivity of Gold Spheroids and Nanorods. *Langmuir* **2002**, *18* (3), 922−927.

(21) Maurin-Pasturel, G.; Long, J.; Guari, Y.; Godiard, F.; Willinger, M. G.; Guerin, C.; Larionova, J. Nanosized Heterostructures of Au@ Prussian Blue Analogues: Towards Multifunctionality at the Nanoscale. *Angew. Chemie - Int. Ed.* **2014**, *53* (15), 3872−3876.
(22) Maurin-Pasturel, G.; Mamontova, E.; Palacios, M. A.; Long, J.; Allouche, J.; Dupin, J. C.; Guari, Y.; Larionova, J. Gold@Prussian Blue Analogue Core-Shell Nanoheterostructures: Their Optical and Magnetic Properties. *Dalt. Trans.* **2019**, *48* (18), 6205−6216.
(23) Torres-Cavanillas, R.; Sanchis-Gual, R.; Dugay, J.; Coronado-Puchau, M.; Giménez-Marqués, M.; Coronado, E. Design of Bistable Gold@Spin-Crossover Core−Shell Nanoparticles Showing Large Electrical Responses for the Spin Switching. *Adv. Mater.* **2019**, *31* (27), No. 1900039.
(24) Sanchis-Gual, R.; Torres-Cavanillas, R.; Coronado-Puchau, M.; Giménez-Marqués, M.; Coronado, E. Plasmon-Assisted Spin Transition in Gold Nanostar@spin Crossover Heterostructures. *J. Mater. Chem. C* **2021**, *9* (33), 10811−10818.
(25) Sakaida, S.; Otsubo, K.; Sakata, O.; Song, C.; Fujiwara, A.; Takata, M.; Kitagawa, H. Crystalline Coordination Framework Endowed with Dynamic Gate-Opening Behaviour by Being Downsized to a Thin Film. *Nat. Chem.* **2016**, *8* (4), 377−383.
(26) Armelles, G.; Cebollada, A.; García-Martín, A.; González, M. U. Magnetoplasmonics: Magnetoplasmonics: Combining Magnetic and Plasmonic Functionalities (Advanced Optical Materials 1/2013). *Adv. Opt. Mater.* **2013**, *1* (1), 10−35.
(27) Turkevich, J. Colloidal Gold. Part I. *Gold Bull.* **1985**, *18* (4), 125−131.
(28) Nikoobakht, B.; El-Sayed, M. A. Preparation and Growth Mechanism of Gold Nanorods (NRs) Using Seed-Mediated Growth Method. *Chem. Mater.* **2003**, *15* (10), 1957−1962.
(29) Wang, Y.; Serrano, A. B.; Sentosun, K.; Bals, S.; Liz-Marzán, L. M. Stabilization and Encapsulation of Gold Nanostars Mediated by Dithiols. *Small* **2015**, *11* (34), 4314−4320.
(30) Pintado, S.; Goberna-Ferrón, S.; Escudero-Adán, E. C.; Galán-Mascarós, J. R. Fast and Persistent Electrocatalytic Water Oxidation by Co-Fe Prussian Blue Coordination Polymers. *J. Am. Chem. Soc.* **2013**, *135* (36), 13270−13273.
(31) Rubio-Giménez, V.; Bartual-Murgui, C.; Galbiati, M.; Núñez-López, A.; Castells-Gil, J.; Quinard, B.; Seneor, P.; Otero, E.; Ohresser, P.; Cantarero, A.; Coronado, E.; Real, J. A.; Mattana, R.; Tatay, S.; Martí-Gastaldo, C. Effect of Nanostructuration on the Spin Crossover Transition in Crystalline Ultrathin Films. *Chem. Sci.* **2019**, *10* (14), 4038−4047.
(32) Chen, Y. C.; Lee, I. L.; Sung, Y. M.; Wu, S. P. Triazole Functionalized Gold Nanoparticles for Colorimetric Cr3+ Sensing. *Sensors Actuators, B Chem.* **2013**, *188*, 354−359.
(33) Yuan, H.; Ji, W.; Chu, S.; Liu, Q.; Qian, S.; Guang, J.; Wang, J.; Han, X.; Masson, J. F.; Peng, W. Mercaptopyridine-Functionalized Gold Nanoparticles for Fiber-Optic Surface Plasmon Resonance Hg 2+ Sensing. *ACS Sensors* **2019**, *4* (3), 704−710.
(34) Brotons-Alcázar, I.; Torres-Cavanillas, R.; Morant-Giner, M.; Cvikl, M.; Mañas-Valero, S.; Forment-Aliaga, A.; Coronado, E. Molecular Stabilization of Chemically Exfoliated Bare MnPS 3 Layers. *Dalt. Trans.* **2021**, *50* (44), 16281−16289.
(35) Zhao, J.; Zhang, J.; Li, Z.; Bu, X. Recent Progress on NiFe-Based Electrocatalysts for the Oxygen Evolution Reaction. *Small* **2020**, *16* (5), No. 2003916.
(36) Jiang, M.; Fan, X.; Cao, S.; Wang, Z.; Yang, Z.; Zhang, W. Thermally Activated Carbon−Nitrogen Vacancies in Double-Shelled NiFe Prussian Blue Analogue Nanocages for Enhanced Electrocatalytic Oxygen Evolution †. *J. Mater. Chem. A* **2021**, *9*, 12734−12745.
(37) Regueiro, A.; Castells-Gil, J.; Shen, C.; Mikulska, I.; Allen, C.; Bogani, L.; Torres-Cavanillas, R. Controlling AxMn[Fe(CN)6] Charge Transfer Pathways through Tilt-Engineering for Enhanced Metal-to-Metal Interactions. *Mater. Adv.* **2024**, *5*, 7473−7480.
(38) Mayer, K. M.; Hafner, J. H. Localized Surface Plasmon Resonance Sensors. *Chem. Rev.* **2011**, *111* (6), 3828−3857.
(39) Sanchis-Gual, R.; Susic, I.; Torres-Cavanillas, R.; Arenas-Esteban, D.; Bals, S.; Mallah, T.; Coronado-Puchau, M.; Coronado, E. The Design of Magneto-Plasmonic Nanostructures Formed by Magnetic Prussian Blue-Type Nanocrystals Decorated with Au Nanoparticles. *Chem. Commun.* **2021**, *57*, 1903−1906.
(40) Larionova, J.; Maurin-Pasturel, G.; Long, J.; Palacios, M. A.; Guérin, C.; Charnay, C.; Willinger, M.-G.; Trifonov, A. A.; Guari, Y. Engineered Au Core@Prussian Blue Analogues Shell Nanoheterostructures: Their Magnetic and Optical Properties. *Chem. - A Eur. J.* **2017**, *23* (31), 7483−7496.
(41) Lee, K. S.; El-Sayed, M. A. Gold and Silver Nanoparticles in Sensing and Imaging: Sensitivity of Plasmon Response to Size, Shape, and Metal Composition. *J. Phys. Chem. B* **2006**, *110* (39), 19220−19225.
(42) Feng, Y.; Wang, X.; Dong, P.; Li, J.; Feng, L.; Huang, J.; Cao, L.; Feng, L.; Kajiyoshi, K.; Wang, C. Boosting the Activity of Prussian-Blue Analogue as Efficient Electrocatalyst for Water and Urea Oxidation. *Sci. Rep.* **2019**, *9* (1), 15965.
(43) Schart, M.; Torres-Cavanillas, R.; Wheeler, S.; Hurlbutt, K.; Manuel, P.; Khalyavin, D.; Zhang, R.; Vincent, D.; Rocquefelte, X.; Volonakis, G.; et al. Nonaqueous Synthesis of Low-Vacancy Chromium Hexacyanochromate. *Inorg. Chem.* **2024**, *63* (48), 22856−22864.
(44) Krah, T.; Ben Amor, N.; Robert, V. Switching Magnetic Interactions in the NiFe Prussian Blue Analogue: An Ab Initio Inspection. *Phys. Chem. Chem. Phys.* **2014**, *16* (20), 9509−9514.
(45) You, B.; Tang, M. T.; Tsai, C.; Abild-Pedersen, F.; Zheng, X.; Li, H. Enhancing Electrocatalytic Water Splitting by Strain Engineering. *Adv. Mater.* **2019**, *31* (17), No. 1807001.
(46) Soriano-López, J.; Steuber, F. W.; Mulahmetović, M.; Besora, M.; Clemente-Juan, J. M.; O'Doherty, M.; Zhu, N. Y.; Hill, C. L.; Coronado, E.; Poblet, J. M.; Schmitt, W. Accelerating Water Oxidation - a Mixed Co/Fe Polyoxometalate with Improved Turnover Characteristics. *Chem. Sci.* **2023**, *14* (47), 13722−13733.
(47) Zhuang, Z.; Giles, S. A.; Jenness, G. R.; Abbasi, R.; Chen, X.; Wang, B.; Vlachos, D. G.; Yan, Y. Oxygen Evolution on Iron Oxide Nanoparticles: The Impact of Crystallinity and Size on the Overpotential. *J. Electrochem. Soc.* **2021**, *168* (3), No. 034518.
(48) Liu, Y.; Wang, S.; Li, Z.; Chu, H.; Zhou, W. Insight into the Surface-Reconstruction of Metal−Organic Framework-Based Nanomaterials for the Electrocatalytic Oxygen Evolution Reaction. *Coord. Chem. Rev.* **2023**, *484*, No. 215117.
(49) Simonov, A.; De Baerdemaeker, T.; Boström, H. L. B.; Ríos Gómez, M. L.; Gray, H. J.; Chernyshov, D.; Bosak, A.; Bürgi, H. B.; Goodwin, A. L. Hidden Diversity of Vacancy Networks in Prussian Blue Analogues. *Nature* **2020**, *578* (7794), 256−260.

https://doi.org/10.1021/acs.inorgchem.4c05320
Inorg. Chem. 2025, 64, 6510−6518